

# Hyperspectral imaging of human prostate tissue with automatic segmentation and histologic validation

Chinmay Patwardhan<sup>a,b</sup>, Kelden Pruitt<sup>a,b</sup>, Ling Ma<sup>a,b</sup>, Douglas W. Strand<sup>c</sup>,  
Payal Kapur<sup>d</sup>, Xiaosong Meng<sup>c</sup>, Brett A. Johnson<sup>c</sup>, Baowei Fei<sup>a,b,e\*</sup>

<sup>a</sup>University of Texas at Dallas, Department of Bioengineering, Richardson, TX

<sup>b</sup>University of Texas at Dallas, Center for Imaging and Surgical Innovation, Richardson, TX

<sup>c</sup>University of Texas Southwestern Medical Center, Department of Urology, Dallas, TX

<sup>d</sup>University of Texas Southwestern Medical Center, Department of Anatomical Pathology, Dallas, TX

<sup>e</sup>University of Texas Southwestern Medical Center, Department of Radiology, Dallas, TX

\* Corresponding author: bfei@utdallas.edu, Website: <https://fei-lab.org>

## ABSTRACT

Hyperspectral imaging (HSI) is an emerging modality that captures rich spatial and spectral information, offering promise for tissue characterization and disease diagnosis. In the context of the prostate, where histopathological assessment remains the gold standard, current imaging techniques often lack sufficient ability to support fine-grained tissue discrimination. Moreover, large annotated HSI datasets are scarce due to the complexity of expert labeling, limiting the development of data-driven diagnostic models. We present a framework for HSI-based analysis of gross prostate datasets, integrating remote annotation for prostate tissue segmentation. HSI data were acquired *ex vivo* from prostate specimens after radical prostatectomy (RP). Three snapshot HSI cameras were utilized for data acquisition, including a visible (VIS), red/near-infrared (RNIR), and near-infrared (NIR) HSI camera. Digitized histological images were matched to corresponding hyperspectral images. A web-based tool was enabled to facilitate remote annotation on whole-slide images. A spatial-spectral transformer architecture was developed to segment different tissue of the prostate. Our preliminary results show that RNIR achieved the pixel accuracy of 0.694 and NIR yielding a Dice similarity coefficient of 0.601, suggesting that the results can be further improved and that HSI may have potential value in the NIR range. This pilot study provides a pipeline for hyperspectral imaging of human prostate tissue with histologic correlation and validation.

**Keywords:** Hyperspectral imaging, prostate cancer, benign prostatic hyperplasia, digital pathology, deep learning, tissue segmentation, spatial-spectral transformer, remote histological annotation

## 1. INTRODUCTION

Radical prostatectomy (RP) is a primary, evidence-based treatment for localized prostate cancer with proven benefit to cancer specific survival. The surgeon's level of experience contributes to the overall patient outcomes due to the high degree of precision demanded by this procedure. Negative tumor margins are desirable as they indicate a complete removal of malignant tissue, whereas, positive surgical margin (PSM) indicates the incomplete removal of cancerous regions, which can result in 2.6-fold increased unadjusted risk to prostate cancer specific mortality.<sup>1,2,3</sup> But negative margins can be difficult to attain without causing neurovascular bundle damage, putting surgeons in difficult positions of balancing removal of localized cancer with simultaneously sparing of essential nerves important for patients' erectile function. The average rate of PSM after RP is upwards of 15% and can increase up to 50% in men with more locally advanced disease.<sup>4</sup> In addition to prostate cancer, elevated biomarkers such as prostate specific antigen (PSA) can be attributed to other benign factors and may require an invasive tissue biopsy to differentiate between the two conditions.<sup>5,6</sup> Benign prostatic hyperplasia (BPH) is a non-malignant but highly prevalent enlargement of the prostate which leads to lower urinary tract symptoms such as increased urinary frequency, urgency, nocturia, and incomplete bladder emptying. BPH may require surgical intervention when frontline pharmacologic such as alpha-blockers and 5 $\alpha$ -reductase inhibitors are not sufficient.

Given the obstacles surrounding nerve-sparing RP and the benefit of minimally invasive surgical removal of BPH, quantitative and objective tools for tumor margin assessment and hyperplasia detection would be of great value. This

study introduces a multi-stage pipeline involving: 1) HSI acquisition using our custom hyperspectral imaging system with three different cameras spanning visible to near-infrared bands,<sup>7</sup> 2) histopathological correlation through remote annotation using the TissUUmeps web application, and 3) self-supervised masked pretraining followed by supervised finetuning of a transformer-based segmentation model. Annotated histological images were manually registered to corresponding hyperspectral images to produce reference maps for histologic validation.

## 2. METHODS

### Image Acquisition

A high-speed HSI system, previously developed by our group,<sup>8,9</sup> was used for all data acquisition. The system includes three HSI cameras covering distinct spectral ranges: visible (VIS, 460–600 nm), red/near-infrared (RNIR, 600–850 nm), and near-infrared (NIR, 665–960 nm). Image acquisition was performed using our homemade software. Optical parameters, including f-number, focal length, exit pupil distance, and integration time were configured for each imaging session. Dark and white reference images were captured before sample imaging for each spectral band, with white reference tiles positioned at approximately the same working distance as the specimens.

### Gross Pathology Prostate Imaging Workflow

Following surgical removal, whole prostates were stored in phosphate-buffered saline (PBS) within sealed containers and transported on dry ice to the imaging lab. Each gland was sectioned into 5–7 axial slices (6 mm thickness) using custom-designed 3D-printed molds, tailored to accommodate anatomical variability. Molds were fabricated from polylactic acid using computer-aided design (CAD) software, with features to ensure precise alignment and even spacing (*e.g.*, guideposts and clamp mechanisms). Sectioning was performed simultaneously using up to six 8-inch razor blades secured in a 3D-printed holder. Each component, including the individual CAD models and the final configuration, can be seen in Figure 1. The orientation of each axial slice was maintained with surgical sutures prior to imaging. Slices were placed on non-reflective, optically absorbing well plates to reduce spectral artifacts. PBS was applied regularly to preserve tissue hydration and minimize specular reflection. Both the superior and inferior surfaces of every section were imaged using the three HSI cameras. A fixed working distance (~6.5 cm) was used to ensure complete specimen inclusion within the field of view. Pathology inking was applied to two opposing surfaces for subsequent histopathological correlation. Post-imaging, pathology ink was applied and allowed to dry before fixation in 10% formalin solution for a minimum of 24 hours.<sup>10</sup> Standard histological processing, including paraffin embedding, microtome sectioning, hematoxylin and eosin (H&E) staining, was performed for each specimen.

### Digital Histology and Annotation

Histology slides were digitized with an Olympus VS200 research slide scanner, generating high-resolution whole-slide images at 4×, 20×, and 40× magnification. OlyVIA© software was used to identify the tissue sections with the highest quality and best alignment as compared to the hyperspectral images. Digitized histological images were then annotated by an experienced pathologist. To enable remote access for annotation, the TissUUmeps platform<sup>11</sup> was deployed using a Docker container. The setup facilitated secure access to high-resolution histological images, allowing the pathologist to remotely view and annotate the images through a web-based interface. To ensure compatibility with the annotation platform, histological images were first converted to OME-TIFF format using the Bio-Formats command-line tool (bfconvert). During conversion, images were exported with a three-level pyramid resolution (scale factor of two) and compressed using JPEG to optimize storage and transfer efficiency. The resulting OME-TIFF files were then transformed into Deep Zoom Image (DZI) format using the libvips image processing library.

The TissUUmeps interface was hosted within a Docker container on a high-performance computer workstation, with the web interface exposed through a local port. Remote access was enabled using the ngrok tunneling service, which provided a static HTTPS endpoint. Basic authentication was configured via ngrok's traffic policy system to restrict unauthorized access. All image data were fully de-identified to maintain patient privacy and confidentiality. After annotation, the segmentation maps were manually registered to the corresponding hyperspectral images to generate a labeled dataset for downstream model training. Class-wise labels were generated using a custom MATLAB script.

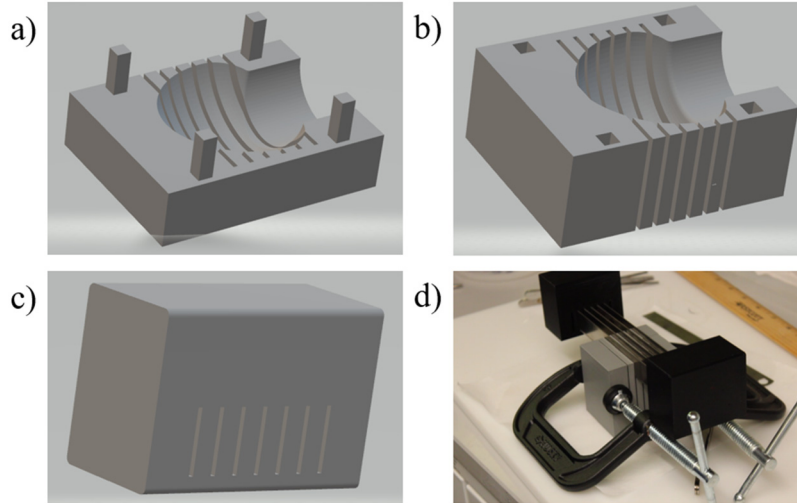


**Figure 1.** Prostate mold components for radical prostatectomy resection handling. (a) Posterior mold piece. (b) Anterior mold piece. (c) Blade holder. (d) Components used in concert on specimen.

### Spatial-Spectral Transformer

A deep learning neural network was developed and implemented to segment different prostate tissues on hyperspectral images. A spatial-spectral model was adapted and modified from a previous work.<sup>12,13</sup> Given the limited availability of HSI data with annotated histological reference images,<sup>14</sup> we used our masked image modeling method for unlabeled hyperspectral images.<sup>13</sup> Mean absolute error (MAE) was used as the reconstruction loss, and training was performed over 300 epochs for each spectral encoder. The resulting pretrained encoders were then incorporated into a segmentation pipeline and finetuned using the annotated subset of the data. A leave-one-out cross-validation (LOOCV) approach was used for model evaluation, with performance reported using pixel-wise accuracy, mean Dice coefficient, and mean intersection over union (IoU). Masked pretraining was conducted using random masking with a masking ratio of 0.8. Due to registration challenges across different hyperspectral cameras, direct hypercube concatenation was not feasible. As a result, individual models were trained for the data acquired by each hyperspectral camera. Spatial patch size was fixed at  $16 \times 16$  pixels, while spectral patch sizes varied in accordance with the spectral resolution of each camera: four bands for the VIS (16 bands) and NIR (24 bands) cameras, and three bands for the RNIR camera (15 bands). Significant model parameters for the transformer are described in Table 1 below.

**Table 1.** Parameters used in transformer models for hyperspectral prostate data.

Dimension	Depth	# Heads	MLP dimension	Dropout
1024	12	12	256	0.1

Variability in imaging conditions, such as slight changes in the distance between camera and tissue (*e.g.*, different height due to tissue curvature) throughout the data collection, introduced difference in the reflectance spectra. To correct these effects, preprocessing was applied to the raw data. First, spectral normalization was performed using the following equation:

$$I'(x, y, \lambda) = \frac{I(x, y, \lambda)}{\sum_{z=1}^N I(x, y, z)}$$

where  $N$  denotes the number of spectral bands. This introduces artificially low values ( $\sim 1/n_{bands}$ ), which suppressed training loss magnitude. Thus,  $Z$ -normalization was subsequently applied using the global mean  $\mu$  and standard deviation  $\sigma$  of the training set:

$$I_z(x, y, \lambda) = \frac{I'(x, y, \lambda) - \mu_{HSI}}{\sigma_{HSI}}$$

where  $\mu_{HSI}$  is the global mean, and  $\sigma_{HSI}$  is the global standard deviation.

To address data scarcity during supervised finetuning, a combinatorial loss function was implemented, composed of weighted cross-entropy and soft Dice loss:

$$\mathcal{L}_{total} = \alpha \mathcal{L}_{CE} + \beta \mathcal{L}_{Dice}$$

with  $\alpha = 0.7$  and  $\beta = 0.3$ .  $\mathcal{L}_{CE}$  and  $\mathcal{L}_{Dice}$  correspond to cross-entropy and Dice loss, respectively. This formulation balanced pixel-level classification with region-level structural agreement, critical for handling class imbalance in segmentation. Class-wise performance metrics were also computed across folds to assess the impact of minority class representation.

### 3. RESULTS

#### Hyperspectral and Histological Dataset

Figure 2 shows the overview of the imaging-to-histology pipeline. In this preliminary study, nine specimens were studied for the correlation between hyperspectral and histological images. The nine selected slides were annotated using the TissUMaps platform, yielding segmentation maps for four distinct tissue classes: benign hyperplasia, prostate zonal anatomy, and stromal nodules. These segmentation masks were registered to their corresponding hyperspectral images and served as ground truth labels for model fine-tuning. Representative examples of these segmentation maps are shown in Figure 3. Hyperplastic regions were predominantly localized to the transition zone while no malignant cancer regions were observed in the nine annotated dataset.

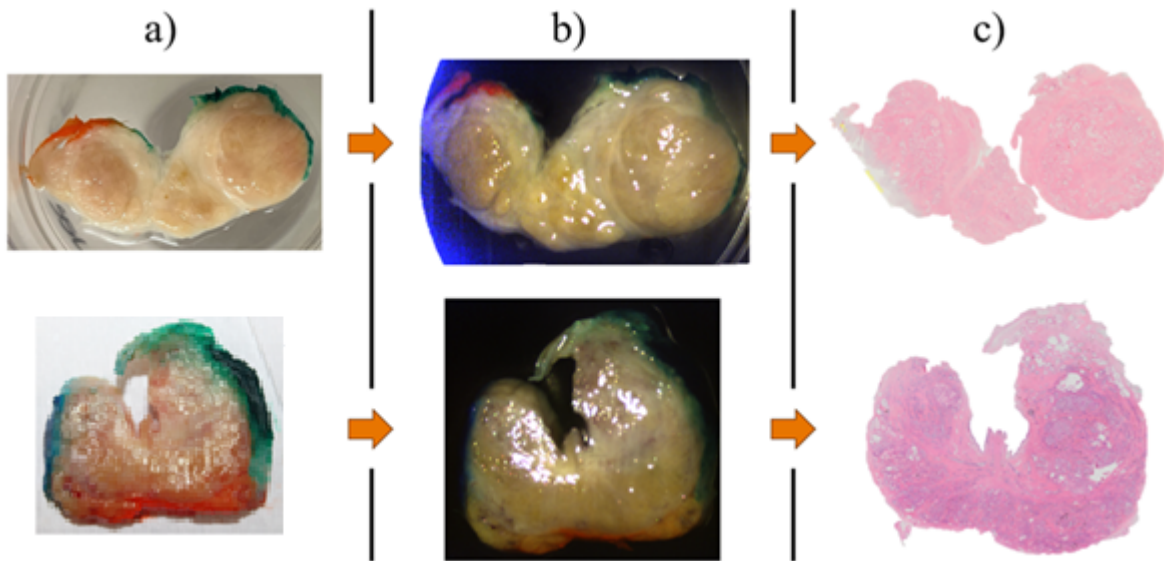


**Figure 2.** Prostate tissue processing and hyperspectral imaging. The top row corresponds to a BPH sample, and the bottom row shows a sectioned prostate specimen. (a) Sliced tissue specimens prior to imaging. (b) Pseudo-RGB images from VIS hyperspectral images. (c) Corresponding digitized histological images of the specimens.

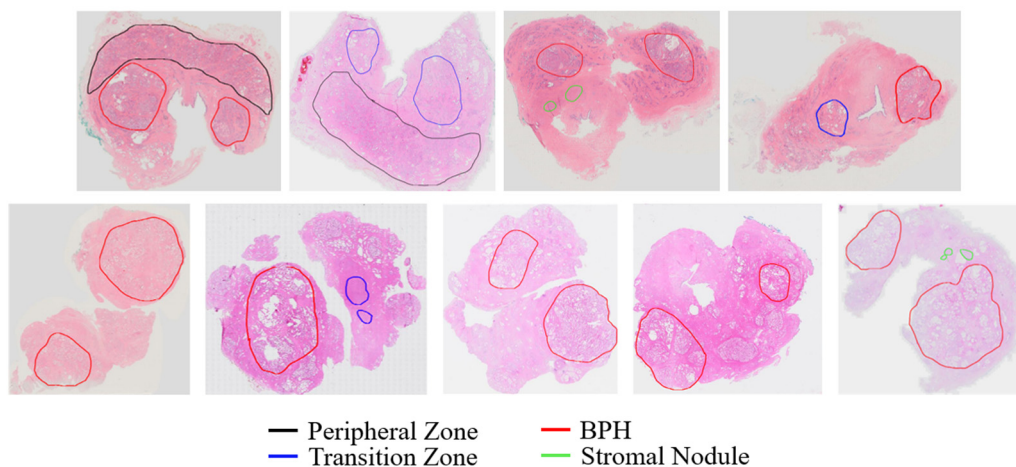


**Figure 3.** Digitized histological images of the specimens from radical prostatectomy (top) and BPH resection (bottom).

### Prostate Tissue Segmentation

Each model was finetuned using a LOOCV scheme, resulting in nine folds corresponding to the nine annotated HSI-histology pairs. Within each training fold, one additional image was held out for internal validation and early stopping. Pixel-wise classification accuracy was used as the criterion for early stopping, with a patience threshold of 25 epochs. The RNIR model achieved the highest mean pixel accuracy across all folds at 0.694, while the NIR model yielded superior region-based performance, attaining the highest mean Dice score coefficient (0.601) and mean IoU (0.541). Table 2 summarizes the evaluation metrics of the segmentation of four classes: Background, Normal, Hyperplasia, and Peripheral. When excluding outlier classes, both RNIR and NIR models demonstrated robust segmentation capabilities, with pixel accuracies ranging from 0.594 to 0.800 and Dice coefficients from 0.470 to 0.859, and IoU values between 0.327 and 0.761.

**Table 2.** Metrics restricted to primary, clinically relevant classes with substantial labeled support (Background, Normal, Hyperplasia, Peripheral). Stromal and Transition are excluded here due to extreme label scarcity.

Class	VIS Pixels	VIS Dice	VIS IoU	VIS Acc.	RNIR Pixels	RNIR Dice	RNIR IoU	RNIR Acc.	NIR Pixels	NIR Dice	NIR IoU	NIR Acc.
Background	16.8k	0.843	0.736	0.780	17,700	0.859	0.761	0.800	17,600	0.779	0.683	0.722
Normal	22k	0.621	0.460	0.635	21,800	0.645	0.493	0.632	21,200	0.653	0.496	0.713
Hyperplasia	7.9k	0.383	0.257	0.518	7,500	0.470	0.327	0.594	8,200	0.296	0.176	0.281
Peripheral	2.5k	0.677	0.511	0.742	2,300	0.553	0.387	0.598	2,300	0.735	0.581	0.799

## 4. DISCUSSION AND CONCLUSION

We developed an end-to-end framework for the curation and analysis of *ex vivo* prostate hyperspectral images with histological validation. 3D printed molds were designed and fabricated to facilitate the controlled sectioning of whole prostate specimens, enabling better spatial correspondence between hyperspectral and histological images. Following tissue sectioning, samples were processed into histological slides and digitized to produce high-resolution pathological images. To support expert annotation of the pathological slides, a remote, web-based platform was implemented, enabling a pathologist to perform tissue segmentation and labeling, thereby providing the histological reference standard for the validation of hyperspectral imaging. Finally, a spatial-spectral transformer network was deployed as the backbone for multi-class prostate tissue segmentation.

Hyperspectral imaging was previously applied to detect prostate cancer in animals *in vivo* and histologic slides.<sup>15</sup> This pilot study established a pipeline for hyperspectral imaging of human prostate tissue with pixel-by-pixel histologic validation. A large study with more specimens and hyperspectral data is warranted to improve and validate the tissue segmentation and correlation methods in the future.

## ACKNOWLEDGMENTS

Research reported in this publication was supported in part by the National Cancer Institute of the National Institutes of Health under Award Number R01CA288379 and the Cancer Prevention and Research Institute of Texas (CPRIT) under Award Number RP240289 and RP240542. The content is solely the responsibility of the authors and does not necessarily represent the official views of the National Institutes of Health.

## REFERENCES

- [1] G. Litjens, O. Debats, J. Barentsz, N. Karssemeijer, and H. Huisman, "SPIE-aapm prostatex challenge data," The Cancer Imaging Archive (2017), doi:10.7937/K9/TCIA.2017.MURS5CL
- [2] O. Yossepowitch, A. Bjartell, J. A. Eastham, M. Graefen, and e. al., "Positive surgical margins in radical prostatectomy: Outlining the problem and its long-term consequences," *Eur. Urol.* **55**(1), 87-99 (2009), <https://doi.org/10.1016/j.eururo.2008.09.030>.
- [3] K. R. Beckmann, M. E. O'Callaghan, A. D. Vincent, and D. Roder, "Clinical outcomes for men with positive surgical margins after radical prostatectomy—results from the south australian prostate cancer clinical outcomes collaborative community-based registry," *BMJ Open* **13**(11), e076070 (2023), <https://doi.org/10.1136/bmjopen-2023-076070>.
- [4] F. Pellegrino, U. G. Falagario, and S. Knipper, "Assessing the impact of positive surgical margins on mortality in patients who underwent robotic radical prostatectomy: 20 years' report from the eau robotic urology section scientific working group," *Eur. Urol. Open Sci.* **52**, 88-95 (2023), <https://doi.org/10.1016/j.euro.2023.07.004>.
- [5] A. Miernik, and C. Gratzke, "Current treatment for benign prostatic hyperplasia," *Dtsch. Arztebl. Int.* **117**(49), 843-854 (2020), <https://doi.org/10.3238/arztebl.2020.0843>.
- [6] P. Crow, A. Molckovsky, N. Stone, J. Uff, K. Wilson, and H. Barr, "Assessment of fiberoptic near-infrared raman spectroscopy for diagnosis of bladder and prostate cancer," *Urol. Oncol.* **23**(1), 15-19 (2005), <https://doi.org/10.1016/j.urolonc.2004.03.003>.
- [7] K. Pruitt, L. Ma, A. Rathgeb, J. C. Gahan, B. A. Johnson, D. W. Strand, and B. Fei, "Design and validation of a high-speed hyperspectral laparoscopic imaging system," *J. Biomed. Opt.* **29**(9), 093506 (2024), <https://doi.org/10.1117/1.JBO.29.9.093506>.
- [8] B. Fei, "Hyperspectral imaging and deep learning for precision surgical intervention," *Molecular-Guided Surgery: Molecules, Devices, and Applications X* 12825, 1282503 (2024). <https://doi.org/10.1117/12.3009170>.
- [9] K. Pruitt, B. Johnson, J. Gahan, L. Ma, and B. Fei, "A high-speed hyperspectral laparoscopic imaging system," *Medical Imaging 2023: Image-Guided Procedures, Robotic Interventions, and Modeling* 12466, 124660G (2023). <https://doi.org/10.1117/12.2653922>.
- [10] G. Lu, L. Halig, D. Wang, Z. Chen, and B. Fei, "Label-free reflectance hyperspectral imaging for tumor margin assessment: A pilot study on surgical specimens of cancer patients," *J. Biomed. Opt.* **22**(8), 086008 (2017), <https://doi.org/10.1117/1.JBO.22.8.086008>.
- [11] L. Solorzano, G. Partel, and C. Wählby, "Tissuumaps: Interactive visualization of large-scale spatial gene expression and tissue morphology data," *Bioinformatics* **36**(15), 4363-4365 (2020), <https://doi.org/10.1093/bioinformatics/btaa541>.
- [12] L. Scheibenreif, M. Mommert, and D. Borth, "Masked vision transformers for hyperspectral image classification," *Proceedings of IEEE/CVF Conference on Computer Vision and Pattern Recognition (CVPR) Workshops*, 2166-2176 (2023). <https://doi.org/10.1109/CVPRW59228.2023.00210>.
- [13] K. Pruitt, H. Pasupuleti, J. Yu, W. DeAtley, and B. Fei, "Masked image modeling in medical hyperspectral imaging: Reconstruction evaluation and downstream tasks," *Proc.SPIE* 13407, 134071G (2025). <https://doi.org/10.1117/12.3048802>
- [14] S. Ortega, M. Halicek, H. Fabelo, G. M. Callico, and B. Fei, "Hyperspectral and multispectral imaging in digital and computational pathology: A systematic review," *Biomed. Opt. Express* **11**(6), 3195-3233 (2020), <https://doi.org/10.1364/BOE.386338>.
- [15] H. Akbari, L. V. Halig, D. M. Schuster, A. Osunkoya, V. Master, P. Nieh, G. Chen, and B. Fei, "Hyperspectral imaging and quantitative analysis for prostate cancer detection," *J. Biomed. Opt.* **17**(7), 076005 (2012), <https://doi.org/10.1117/1.JBO.17.7.076005>.